Article ID: 1006-8775(2023) 02-0204-12

Comparison of Microphysical Characteristics of Warm-sector, Frontal and Shear-line Heavy Rainfall During the Pre-summer Rainy Season in South China

XIA Feng (夏 丰)[1], LIU Xian-tong (刘显通)[1], HU Sheng (胡 胜)[1], LI Hui-qi (黎慧琦)[1], RAO Xiao-na (饶晓娜)[1], LIN Qing (林 青)[2], XIAO Hui (肖 辉)[1], FENG Lu (冯 璐)[1], LAI Rui-ze (赖睿泽)[1]

(1. Guangzhou Institute of Tropical and Marine Meteorology, China Meteorological Administration, Guangzhou 510641 China; 2. Guangdong Meteorological Observatory, China Meteorological Administration, Guangzhou 510641 China)

Abstract: Warm-sector heavy rainfall (WR), shear-line heavy rainfall (SR), and frontal heavy rainfall (FR) are three types of rainfall that frequently occur during the pre-summer rainy season in south China. In this research, we investigated the differences in microphysical characteristics of heavy rainfall events during the period of 10-15 May 2022 based on the combined observations from 11 S-band polarimetric radars in south China. The conclusions are as follows: (1) WR has the highest radar echo top height, the strongest radar echo at all altitudes, the highest lightning density, and the most active ice-phase process, which suggests that the convection is the most vigorous in the WR, moderate in the FR, and the weakest in the SR. (2) Three types of rainfall are all marine-type precipitation, the mass-weighted mean diameter (D_m, mm) and the intercept parameter (N_w, $mm^{-1} m^{-3}$) of the raindrops in the WR are the largest. (3) The WR possesses the highest proportion of graupel compared with the FR and SR, and stronger updrafts and more abundant water vapor supply may lead to larger raindrops during the melting and collision-coalescence processes. (4) Over all the heights, liquid and ice water content in the WR are higher than those in the SR and FR, the ratio of ice to liquid water content in the WR is as high as 27% when ZH exceeds 50 dBZ, definitely higher than that in the SR and FR, indicating that the active ice-phase process existing in the WR is conducive to the formation of heavy rainfall.

Key words: microphysical characteristic; S-band polarimetric radar; warm-sector heavy rainfall; frontal heavy rainfall; shear-line heavy rainfall

CLC number: P426.61+1 **Document code:** A

Citation: XIA Feng, LIU Xian-tong, HU Sheng, et al. Comparison of Microphysical Characteristics of Warm-sector, Frontal and Shear-line Heavy Rainfall During the Pre-summer Rainy Season in South China [J]. Journal of Tropical Meteorology, 2023, 29(2): 204-215, https://doi.org/10.46267/j.1006-8775.2023.016

1 INTRODUCTION

South China is located in the low latitude region, with intense solar radiation, strong East Asian summer monsoon, complex atmospheric circulation, and special coastal terrain, and the rainfalls in this region are changeable, instantaneous, intense, and lengthy (Zhang et al. [1]). The precipitation amount between the period from April to June (known as the pre-summer rainy season) accounts for 40%−50% of the total precipitation each year in south China (Wu et al. [2]). Before and after the onset of the summer monsoon, due to the particular configurations of atmospheric circulation, the rainfalls in south China gradually change from frontal rainstorms to monsoon rainstorms (Liang et al. [3]). In general, the rains are diverse and complex, and the coexistence of shear-line heavy rain (SR), warm-sector heavy rain (WR), and frontal heavy rain (FR) frequently occur (Luo et al. [4]).

The definition of the WR was proposed by Huang et al. [5] in 1986 when they classified the pre-summer rainy season rainfall in south China. It refers to rainstorms that occur on the side of a warm sector 200−300 km away from a surface front, or in the absence of a significant shear at the confluence of westerly and easterly winds. The triggering factors of the WR are complex (He et al. [6]; Sun et al. [7]), warm and humid atmosphere (Wu et al. [8], Zheng et al. [9]), surface sensible / latent heating (Yin et al. [10]), special topographies (Wu et al. [8]; Zhong et al. [11]; Wu et al. [12]), thermal differences between the land and sea (He et al. [6]; Sun et al. [7]), low-level jet (Sun et al. [7]; Wu et al. [12]; Liang et al. [13]), the release of condensation latent heat of water vapor (He et al. [6]), surface cooling effect (Wu et al. [14]), favorable circulation structure (Zheng et al. [9]; Zhao et al. [15]), and weak cold air intrusion (Sun et

Received 2022-09-19; **Revised** 2023-02-15; **Accepted** 2023-05-15

Funding: National Natural Science Foundation of China (U2242203, 41975138, 41905047, 42030610); the High-level Science and Technology Journals Projects of Guangdong Province (2021B1212020016); Natural Science Foundation of Guangdong Province (2019A1515010814, 2021A1515011415); Science and Technology Research Project of Guangdong Meteorological Bureau (GRMC2020M01); the Joint Research Project for Meteorological Capacity Improvement (22NLTSQ003)

Biography: XIA Feng, Research Associate, primarily undertaking research on radar meteorology.

Corresponding author: LIU Xian-tong, e-mail: xtliu@gd121.cn

al.[7]; Zheng et al.[9]; Wang et al.[16]) may be related. Typically, the precipitation intensity of the WR is 3−5 times that of the SR, for which the area is smaller, and the scale is only tens to hundreds of kilometers (Lin [17]).

For the FR, when the East Asian summer monsoon arrives, the cold air originating from northwestern China and the water vapor from the western Pacific Ocean collide over southern China (Zheng et al.[18]). The temperature difference between the two types of air masses is large (Liu and He [19]), lighter warm and moist air is lifted above the cold air on a large scale, and the water vapor is cooled and condensed to form frontal rain (Zheng et al.[18]).

For the SR, the temperature difference between the two sides of a shear line near the low altitude (700−850 hPa) is not obvious, but the horizontal shear of the wind is large. When the northern side of the shear line is dominated by easterly winds and the southern side by southerly winds, water vapor content in the flow will be abundant and a shear vortex is likely to occur. At this time, the airflow will converge to facilitate the accumulation and uplift of water vapor, resulting in the occurrence of heavy rainfall on a large scale (Larson [20]). Since the atmospheric circulation and microphysical properties of SR are different from those of WR and FR, we decided to perform some additional comparative analysis of the microphysical properties of these three types of precipitation.

The differences in the structure of atmospheric thermodynamics and dynamics will lead to different types of rainfall, as well as different development and evolution processes of mesoscale convective systems (MCS) and microphysical characteristics of rainfalls (Wen et al.[21]; Han et al.[22]; Lai et al.[23]). Based on the measurements of polarization radar, Li et al.[24] identified that the record-breaking May 7 extremely heavy rainfall process in Guangzhou in the pre-summer rainy season of 2017 was primarily produced by a warm rain process. The sufficient supply of warm and moist airflow makes the rainfalls in south China in the pre-summer rainy season have the features of a low mass center and warm rain process, resulting in higher precipitation efficiency (Fu et al.[25]). Based on the polarization radar, Huang et al.[26] found that in the extreme rainstorms in south China, the liquid water content under the 0 ℃ level increased rapidly, mainly through the warm rain process, and the raindrops mainly grew through the collision process. Han et al.[22] studied the microphysical characteristics of two types of rainfall in south China and obtained that the coastal WR has stronger convective intensity and larger raindrop size than the inland FR.

During 10−15 May 2022 (Local Standard Time (LST), the same hereafter), a persistent rainfall event occurred in south China, in which the SR, WR, and FR were observed successively. As this event had additional types of rainfall and longer duration than in Han's research, this precipitation process was selected for additional comparative analysis of the microphysical properties of different types of precipitation in southern China. Based on the detection of 11 S-band polarimetric radars in Guangdong province, this study compared the microphysical characteristics of three types of rainfall events: SR, WR, and FR, in an attempt to reveal the different microphysical characteristics of those rainfall events during the pre-summer rainy season in south China.

2 DATA AND METHODS

2.1 *Quality control of S-band polarimetric weather radar data and convective cell identification algorithm*

By 2022, all S-band Doppler weather radars in Guangdong have upgraded their polarization functions. The major radar parameters, such as the radar reflectivity (Z_H, dBZ), differential reflectivity (Z_{DR}, dB), and the specific differential phase shift (K_{DP}, ° km^{-1}), have been discussed in related studies (Chen et al.[27, 28]; Xia et al.[29]; Liu et al.[30]). The yellow dots in Fig. 1 represent the spatial distribution of the 11 S-band polarimetric radars. The observation range of each radar is 230 km. When all radars are networked, they can cover the entire territory of Guangdong province and the coastal areas, forming multiple coverage for various types of rainfall (Li et al.[31]).

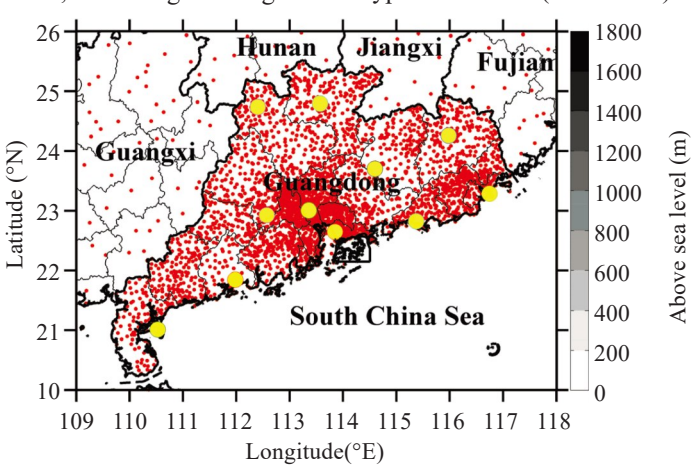

Figure 1. Spatial distribution of S-band polarimetric radars (yellow dots) and automatic weather station rain gauges (red dots).

To obtain high-reliability radar data, quality control of radar echoes was carried out to eliminate non-precipitation echoes referring to previous schemes (Liu et al.[30]; Wu et al.[32]; Wang et al.[33]), including ground clutter, clear sky echo, and abnormal beam. The Z_{DR} system error of each radar was corrected by the micro raindrop method (Liu et al.[30]), then the radar data were gridded and interpolated into 3-D Cartesian coordinates. The horizontal resolution of the interpolated data is 250 m, and the vertical resolution is 500 m (Han et al.[22]; Yu et al.[34]).

According to the convective cell (CC) identification method (Han et al.[22]; Wang et al.[33]), if the Z_H exceeds 40 dBZ in more than one-third of the grid points, it was considered a CC. The echoes were counted from 500 m, taking into account that some radars lacked scans at low altitudes.

2.2 *Automatic weather station data, lightning data, and ERA5 reanalysis data*

Hourly precipitation data were detected from 477 national automatic weather stations (AWSs) in south China and 3388 regional AWSs in Guangdong province from May 10−15, 2022 (red dots in Fig. 1). The quality of precipitation data was controlled by excluding accumulated observation time that was less than 95%. The lightning data was extracted from the Guangdong-Hongkong-Macao lighting location system (GHMLLS), which is the most influential professional lightning location system in Guangdong, recording the time, location, strength, cloud flash, and ground flash of lightning. The environmental conditions of this rainfall event were analyzed by the European Center for Medium-Range Weather Forecasts (ECMWF) fifth-generation hourly reanalysis data (ERA5) with a spatial resolution of 0.25 ° × 0.25 °.

2.3 *Retrieval of raindrop size distribution parameters, estimation of liquid and ice water content, and hydrometeor classification algorithm*

Since 2016, seven 2D-Video Distrometers (2DVDs) have been deployed by the Longmen Field Experiment Base for Cloud Physics of China Meteorological Administration in the coastal and inland rainstorm-prone areas of Guangdong (Liu et al.[35]). By scanning the shape, size, and final velocity of raindrops, the raindrop size distribution (RSD) of different types of rainfall can be obtained (Lai et al.[23]; Feng et al.[36, 37]; Ding et al.[38]). With the long-term RSD data and the S-band polarimetric radar variables, the inversion relation between them can be obtained. In this study, the constrained Gamma distribution model was applied to retrieve the RSD data based on the S-band polarimetric radar observations (Liu et al.[30]). The parameters of raindrop mass-weighted mean diameter (D_m, mm) and the logarithmic-normalized intercept ($\log_{10}N_w$, the unit of N_w is $mm^{-1}\ m^{-3}$) were calculated from the retrieved Gamma raindrop size distribution. The Z_{DP}-R method was adopted to retrieve liquid water content (LWC) and ice water content (IWC) in this study (Li et al.[39]). The hydrometeors were classified by the algorithm described by Park et al.[40] and optimized by Wu et al.[32]. Ultimately, the radar echoes were divided into ten categories: (a) ground clutter (GC); (b) biological scatters (BS); (c) dry snow (DS); (d) wet snow (WS); (e) ice crystal (CR); (f) graupel (GR); (g) big drops (BD); (h) light and moderate rain (RA); (i) heavy rain (HR); and (j) a mixture of rain and hail (RH), only meteorological radar echoes (excluding GC and BS) were used in this study.

3 OVERVIEW OF THE THREE HEAVY RAINFALL PROCESSES

3.1 *Synoptic analyses*

At 1400 LST on May 10, at 850 hPa (Fig. 2a), southwesterly-westerly winds dominated over Guangdong. A shear line was located in the southern province of Hunan. A surface front was located in northern Guangdong, and Guangdong was mainly affected by the southerly winds near the surface (Fig. 2d). At 2100 LST, as the low equivalent potential temperature (θ_e) air in northern Guangdong gradually advanced southwards, the 850 hPa shear line (Fig. 2b) and the surface front (Fig. 2f) moved southwards. It is worth noting that the shear line is one of the major precipitation weather systems, and it frequently cooperates with the surface frontal systems. On the shear line, there is commonly a horizontal convergence and upward motion of the airflow, providing dynamical conditions for the development of precipitation. In this event, at 850 hPa (Fig. 2a-2b), the temperature difference of the airflow on both sides of the shear line was slight, but there was evidently opposite wind speed (northerly winds on the north side and westerly-southwesterly winds on the south side), which caused the convergence of the cold and warm air on the ground in northern Guangdong, and finally, the FR occurred near the surface front and the south of the shear line.

From 2100 LST, it can also be seen that the low-level winds over the coast of Guangdong and the sea adjacent to it gradually strengthened (Fig. 2c-2d, 2f-2g). The winds near the Pearl River Estuary changed to be southerly (Fig. 2f-2g). The intensification of the southerly component enhanced the wind speed convergence and orographic uplift near the coast (Figs. 2f and 3b). At this time, more convection was initiated near the Pearl River Estuary. During this period, coastal precipitation was more than 200 km away from the surface front (Figs. 2f and 3b), having typical WR precipitation characteristics (Huang et al.[5]; Wu et al.[12]). Therefore, the period from 2100 LST on May 10 to 1100 LST on May 11 was chosen as the WR period.

After that, the low θ_e air in northern Guangdong further moved southwards (Fig. 2g-2h). At 1200 LST on May 13, the front moved to central and southern Guangdong (Fig. 2h). From the meridional cross-section

of the equivalent potential temperature and winds, the southward movement of the front can be distinctly seen (Fig. 3). At 1200 LST on May 11, the distance between the front and the coastal precipitation area was less than 200 km. The convection was concentrated in the east of the Pearl River Estuary and was governed by the FR.

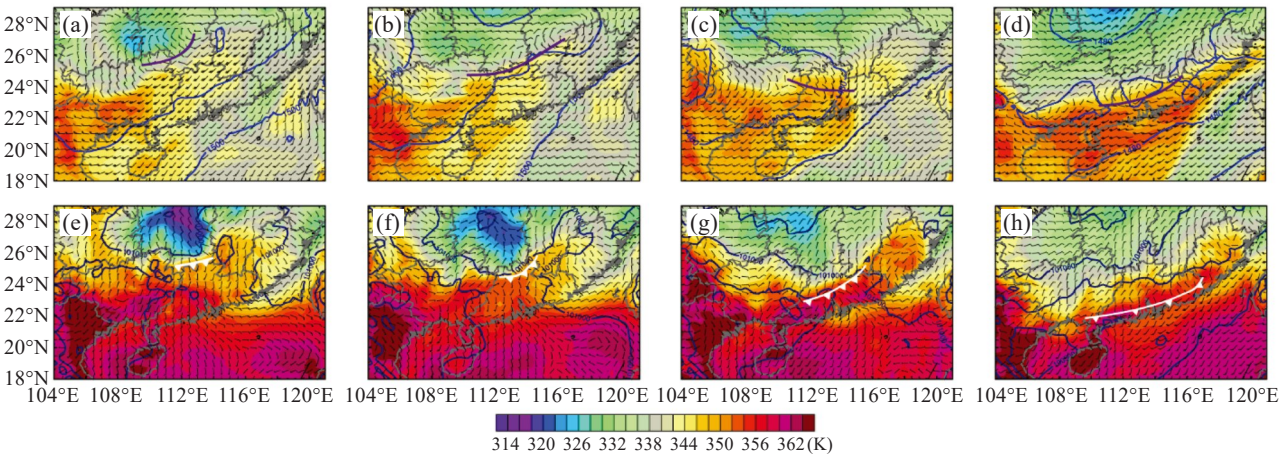

Figure 2. (a-d) Winds, equivalent potential temperature (colored), and geopotential height (blue contours) at 850 hPa. The purple line indicates the location of the shear line. (e-h) 10-m winds, 2-m equivalent potential temperature (colored), and mean sea level pressure (blue contours). White lines with triangles indicate the location of the surface front. The first column is 1400 LST on May 10; the second column is 2100 LST on May 10; the third column is 1200 LST on May 11; and the fourth column is 1200 LST on May 13.

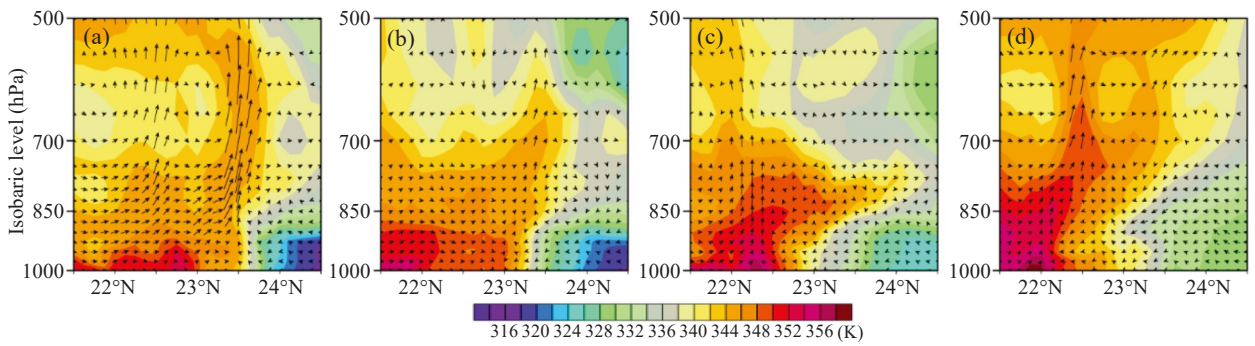

Figure 3. Cross-section along 112°E of equivalent potential temperature (colored), meridional wind, and vertical wind (vertical wind speed multiplied by 100). (a) 1400 LST on May 10; (b) 2100 LST on May 10; (c) 1200 LST on May 11; and (d) 1200 LST on May 13.

3.2 *Precipitation processes*

Figure 4a shows the distribution of total precipitation determined from the AWSs in south China for the entire precipitation event. Rainfall was mainly in coastal and central inland areas over Guangdong, where accumulations reached 200−800 mm and 400−600 mm, respectively.

According to the synoptic situation (Figs. 2 and 3), accumulated precipitation of AWSs (Fig. 4), and reflectivity observations (Fig. 5), the SR region was mainly distributed in central inland Guangdong (red box in Fig. 4b). On both sides of the SR, the wind direction and velocity at 850 hPa were relatively different. The regional MCS governed the rainfall, and the rain bands were elliptical. The duration of the rain was mainly from 1400 LST on May 10 to 0200 LST on May 11, with a maximum accumulation of 150−200 mm. The WR mainly occurred on the west coast of Guangdong (red box in Fig. 4c) and featured a linear mesoscale convective system (MCS) parallel to the coastline. The main duration of the rainfall was from 2100 LST to 1100 LST on May 10, with accumulations reaching 200−300 mm. The FR region was close to the inland area of the coast (red box in Fig. 4d), the main duration was from 1200 LST to 2400 LST on May 13, and the maximum accumulated precipitation was 100−200 mm.

4 DIFFERENCES IN THE VERTICAL STRUCTURE

The time-height distributions of the mean Z_H, Z_{DR} and K_{DP} of the convective cells (CCs) for the three types of rainfall (WR, SR, and FR) are shown in Fig. 6. The mean Z_H of CCs for three types of rainfall were all higher than 40 dBZ below the 0 ℃ level. However, the distribution range of high Z_H values was found to be most widely distributed in the WR (Fig. 6b), less in the FR (Fig. 6a), and least in the SR (Fig. 6c). These indicate that Z_H is the strongest in the WR, followed by

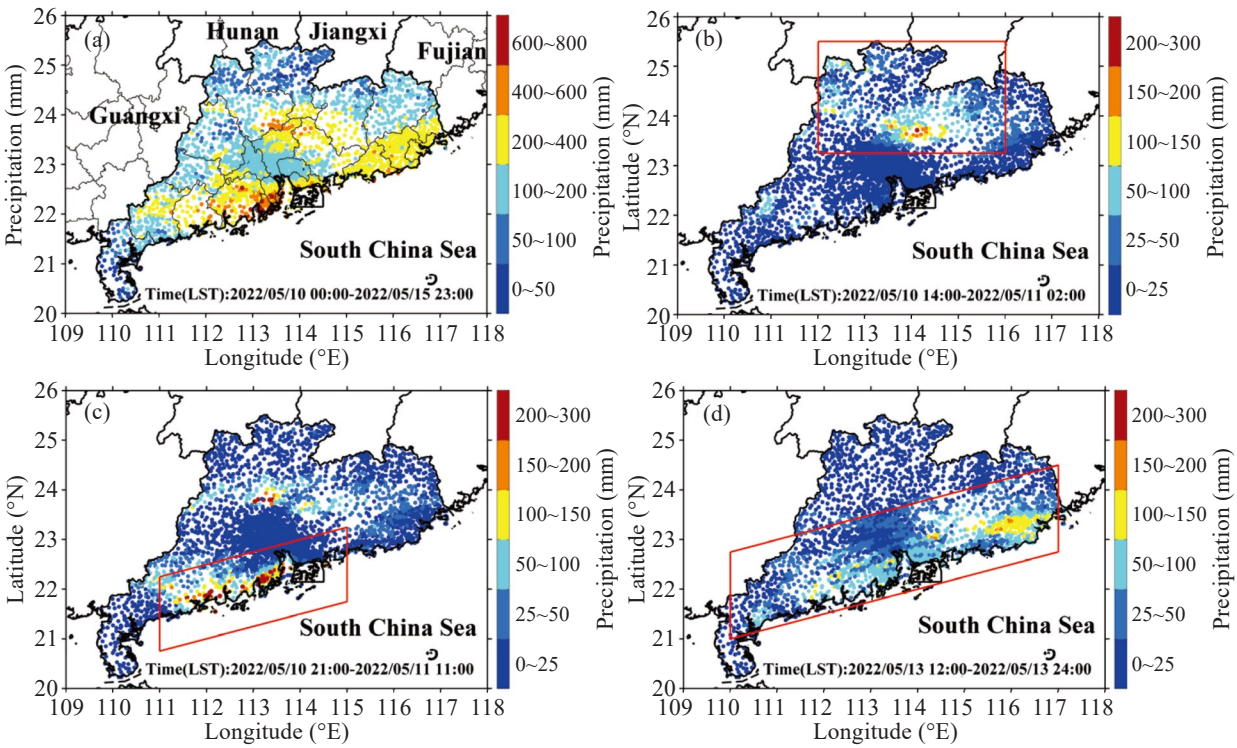

Figure 4. (a) Total precipitation from 10-15 on May 2022 and accumulated precipitation for the three types of rainfall of (b) SR, (c) WR, and (d) FR.

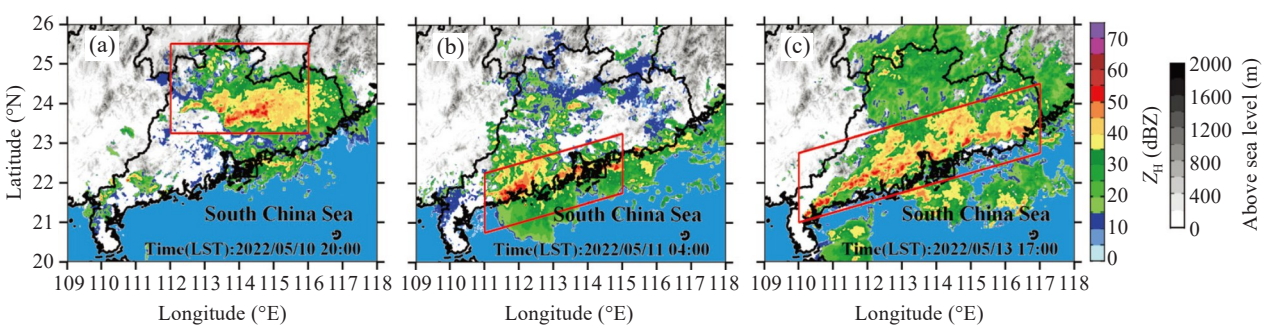

Figure 5. The radar reflectivity data from a 3-km constant altitude plan position indicator (CAPPI) of (a) SR, (b) WR, and (c) FR. The red boxes indicate the corresponding rainfall areas.

the FR and the weakest in the SR. The Z_{DR} increased as the height decreased in the WR, and the averaged Z_{DR} in the WR (Fig. 6d) reached a maximum of 0.5−1.0 dB below the 0 °C level. To liquid raindrops, a larger Z_{DR} suggests a larger average raindrop diameter. This shows that the average size of raindrops in WR CCs increases during the rainfall. The average K_{DP} in the WR (Fig. 6h) was the largest, reaching a maximum of 0.5−1.5 ° km^{-1} below the 0 °C level, obviously larger than those in the SR and FR. The S-band polarimetric radar quantitative precipitation estimation (QPE) algorithm (Guo et al. [41]; Zhou et al. [42]) shows that K_{DP} is closely related to rainfall intensity. A larger K_{DP} indicates larger precipitation. Thus, the rainfall intensity in the WR was significantly stronger than that in the SR.

Figure 7a-7c shows the maximum height of Z_H for the three types of rainfall with different intensities. The red curve represents the Z_H for 40 dBZ, and the blue curve represents the Z_H for 20 dBZ. As shown in Fig. 7, the Z_H for 20 dBZ and 40 dBZ reached up to 16−20 km and 10−14 km in the WR, respectively, followed by 14−18 km and 8−12 km in the FR alone. The maximum Z_H heights in the SR were the lowest at 20 dBZ and 40 dBZ. These indicate that the convection in the WR was most intense during this rainfall event.

Figure 7d-7f shows the proportion of the CCs area versus the rainfall area and the lightning density in the SR, WR, and FR, and the proportion of the CCs area was calculated as follows: CCs areas versus areas with Z_H > 20 dBZ. As shown in Fig. 7, the area of CCs in the WR was the largest. The averaged (maximum) ratio was 6.2% (13.1%) in the WR, 4.6% (6.9%) in the FR, and 3.8% (7.5%) in the SR. Meanwhile, the lightning density in the WR was higher than that in the FR and SR. The

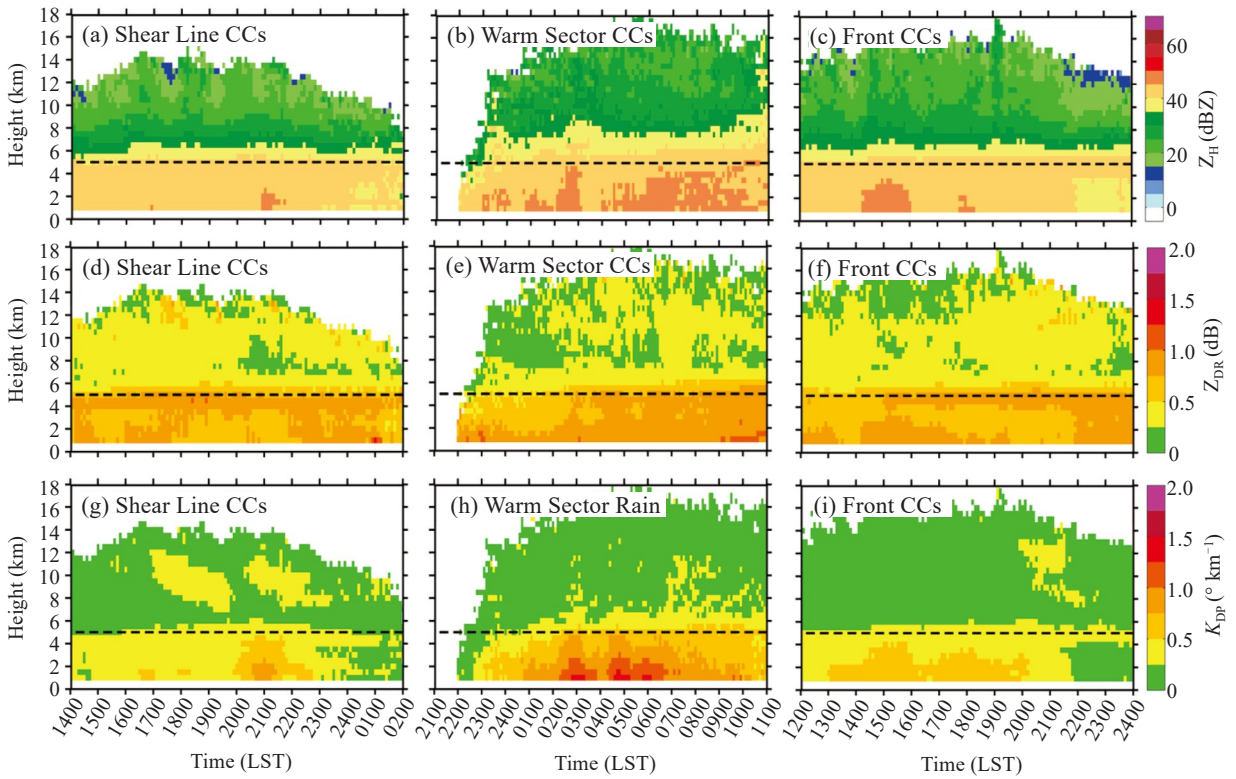

Figure 6. Time-height distributions of the mean Z_H, Z_{DR}, and K_{DP} of CCs of three types of rainfall. (a, d, g): SR, (b, e, h): WR, and (c, f, i): FR.

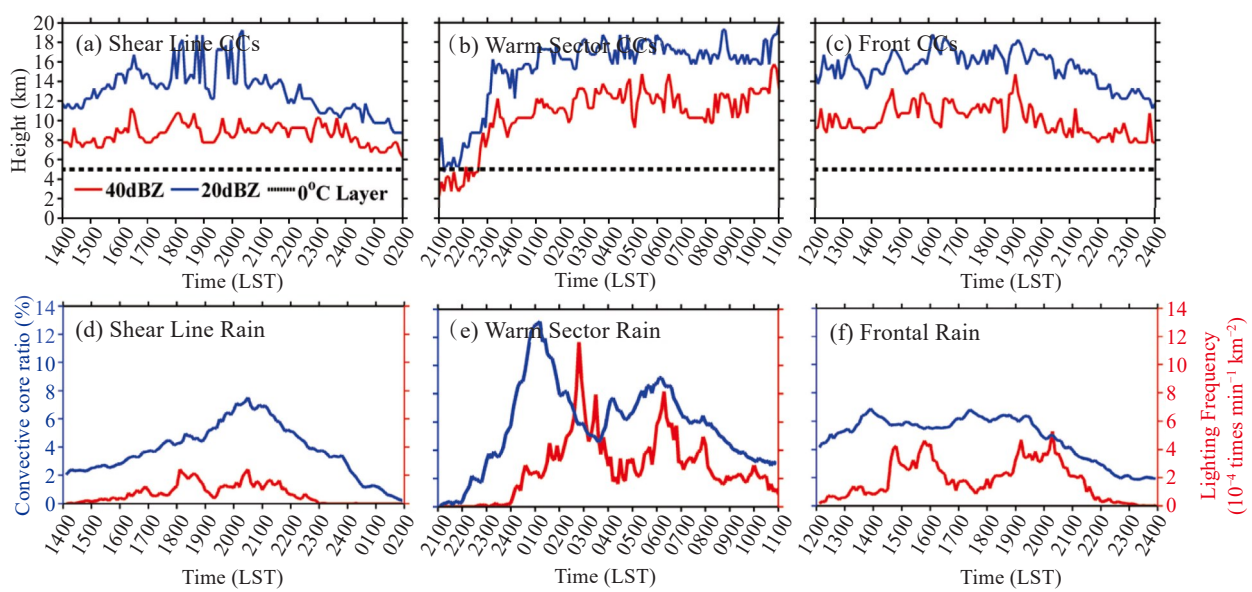

Figure 7. The Z_H heights at 20 dBZ and 40 dBZ for the three types of rainfall of (a) SR, (b) WR, and (c) FR, and the ratio of CCs area versus rainfall area (units: %) and the lightning density for the three types of rainfall (units: 10^{-4} times min^{-1} km^{-2}) of (d) SR, (e) WR, and (f) FR.

averaged (maximum) lightning density was 3.0 (11.7)× 10^{-4} times min^{-1} km^{-2} in the WR, and was 1.5(5.3)×10^{-4} times min^{-1} km^{-2} in the FR, and only 0.6(2.4) ×10^{-4} times min^{-1} km^{-2} in the SR. It can be seen from CCs ratio and lightning density that the convective updrafts in the WR was the most vigorous, followed by the FR, and the SR was the weakest.

Furthermore, we compared the rainfall rates of different Z_H (Fig. 8a-8c) and the probability density distributions of 20 dBZ (solid lines) and 40 dBZ (dashed lines) radar echo heights in the CCs for the three types of rainfall (Fig. 8d-8f). The maximum Z_H of the CCs was classified into three grades (40−45 dBZ, 45−50 dBZ, and >50 dBZ). For all the three types of rainfall, a higher

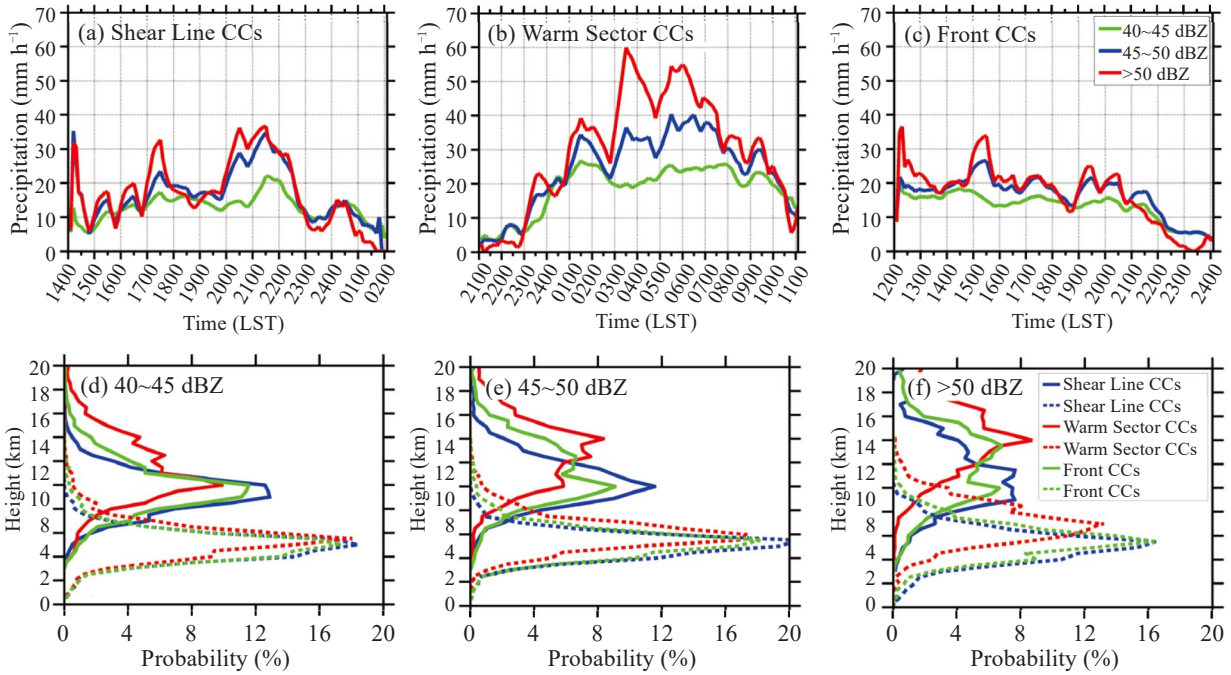

Figure 8. Rainfall rates of different Z_H (a, b, c), probability density distribution (units: %) of 20 dBZ (solid lines) and 40 dBZ (dashed lines) radar echo height (d, e, f), and the maximum Z_H of CCs were divided into three grades (40-45 dBZ, 45-50 dBZ, and > 50 dBZ). The three types of rainfall are SR, WR, and FR.

Z_H value corresponds to higher precipitation intensity. In addition, with identical echo classification, the precipitation intensity in the WR was larger than in the other two types of rainfall. As can be seen from Fig. 8d-8f, the height of the probability density distribution of 20 dBZ and 40 dBZ radar echo heights in the WR was the highest, followed by the FR, and the height of the SR was the lowest.

To exhibit the differences in microphysical features of the SR, WR, and FR more distinctly, the contoured frequency by altitude diagrams (CFADs) (Fig. 9a-9c, 9e-9f, and 9i-9k) and their profile distributions (Fig. 9d, 9h, and 9l) of radar variables were analyzed. The Z_H of the WR (Fig. 9a-9c) was mainly distributed between 40−50 dBZ below the 0 ℃ level, and the Z_H of the SR and FR was mainly distributed between 40−46 dBZ. The vertical profile of Z_H is closely related to the storm intensity in the previous analysis (Han et al. [22]; Li et al. [24]; Wang et al. [33]). As shown in Fig. 9d, the Z_H in the WR was larger than that in the SR and FR at all altitudes, indicating that the convection intensity of the WR was most vigorous in this event. The vertical profile values of Z_H in the FR were slightly higher than in the SR.

As can be seen from the CFADs of Z_{DR} (Fig. 9e-9g) and vertical profile (Fig. 9h), the Z_{DR} of the three types of rainfall increased rapidly as the height decreased from 7 km to 4 km. Below 3 km, the mean Z_{DR} changed little in the SR, while it continued to increase in the WR and FR, from 0.7 dB to 0.9 dB and from 0.65 dB to 0.78 dB, respectively, as the altitude decreased. This means that the average size of the raindrops increased at heights below 3 km in the WR and FR. Combined with the variation of the mean value of the Z_H, it can be found that there were clear collision-coalescence processes in the WR and FR below the 3-km altitude, especially for the WR. For SR, however, it is likely that the raindrop breakup and coalescence processes tended to be equilibrated. This may be related to more abundant water vapor and stronger updrafts in the WR and FR where raindrops become larger with the support of stronger air currents.

Below the 0 ℃ level, the K_{DP} was mainly distributed between 0−1.6 ° km^{-1} in the WR (Fig. 9j), and between 0−1.0 ° km^{-1} in the SR (Fig. 9i) and FR (Fig. 9k). The mean K_{DP} for the three types of rainfall increased rapidly with the height decreasing below the 0 ℃ level. The K_{DP} increased from 0.6 ° km^{-1} to 1.05 ° km^{-1} in the WR (Fig. 9l), and from 0.37 ° km^{-1} to 0.47 ° km^{-1} in the SR (Fig. 9l), and from 0.37 ° km^{-1} to 0.54 ° km^{-1} in the FR (Fig. 9l). From 1 to 6 km in height, the vertical profile values of the K_{DP} in the WR were significantly larger than those in the SR and FR. For pure liquid precipitation, a larger K_{DP} indicates stronger rainfall intensity. It can be concluded that the intensity of rain in the WR was considerably larger than that in the SR and FR.

5 DIFFERENCES IN MICROPHYSICAL CHARACTERISTICS

The RSD is directly related to the condensation, coalescence, evaporation, and falling velocities of hydrometeors and is the most influential parameter affecting microphysical processes in clouds. The joint probability density distributions of the D_m and $\log_{10}N_w$

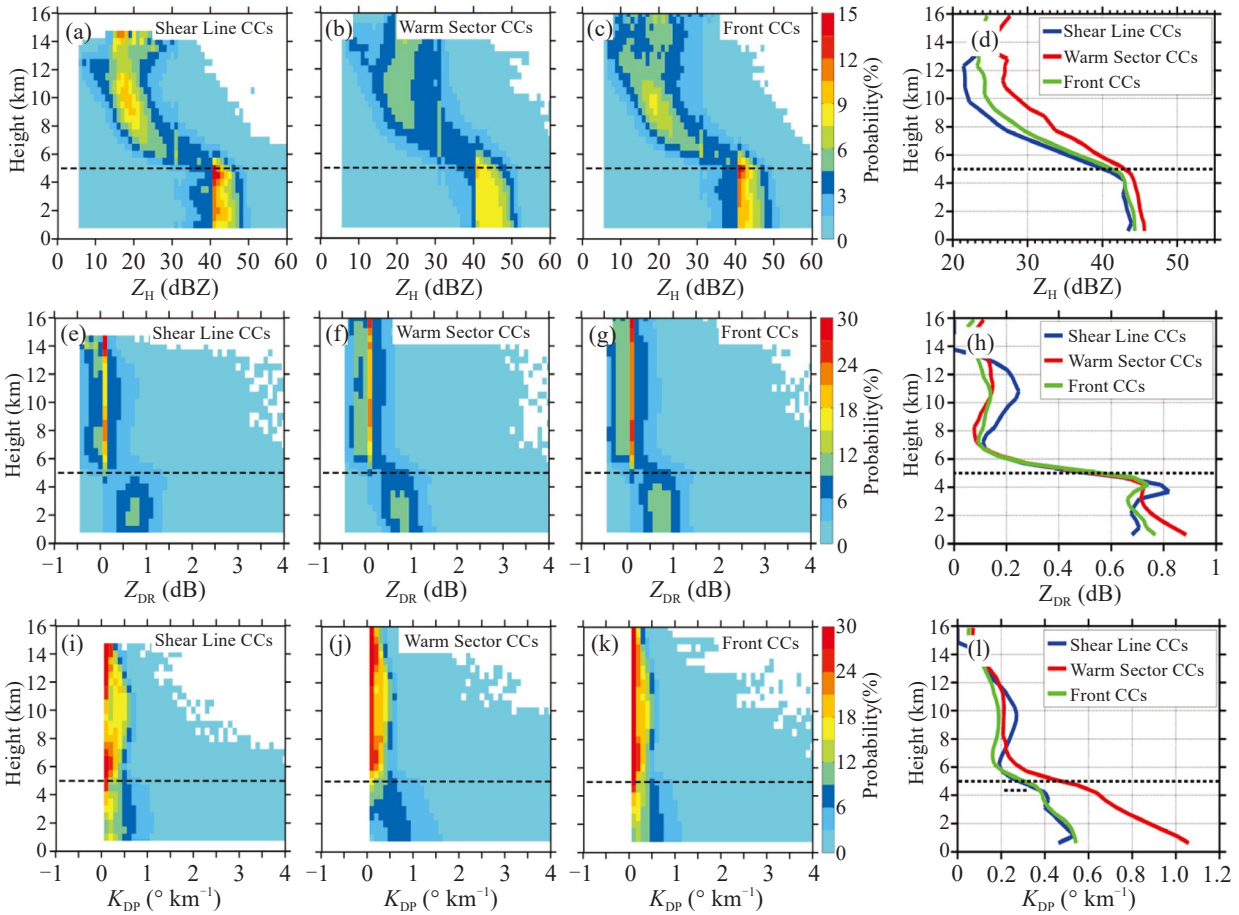

Figure 9. The contoured frequency by altitude diagrams (CFADs) (units: %) of Z_H, Z_{DR}, and K_{DP} of the CCs for the three types of rainfall (a-c, e-f, i-k), and corresponding vertical profile distributions (d, h, l) for the three types of rainfall of SR, WR, and FR.

parameters for the three types of precipitations retrieved from the S-band dual-polarization radars at altitudes below 2 km are shown in Fig. 10. Here, D_m denotes the average raindrop size, and N_w is related to the concentration of raindrops. The statistical results of D_m and $\log_{10}N_w$ show that the three types of rainfall belonged to marine-type precipitation (Feng et al.[36, 37]). Specifically, the average value of D_m and N_w in the WR were the largest (1.6 mm, 4.28 mm^{-1} m^{-3}), the SR (1.53 mm, 4.23 mm^{-1} m^{-3}) and the FR were close (1.55 mm, 4.22 mm^{-1} m^{-3}). These suggest that raindrop sizes and number concentrations were larger in WR than in SR

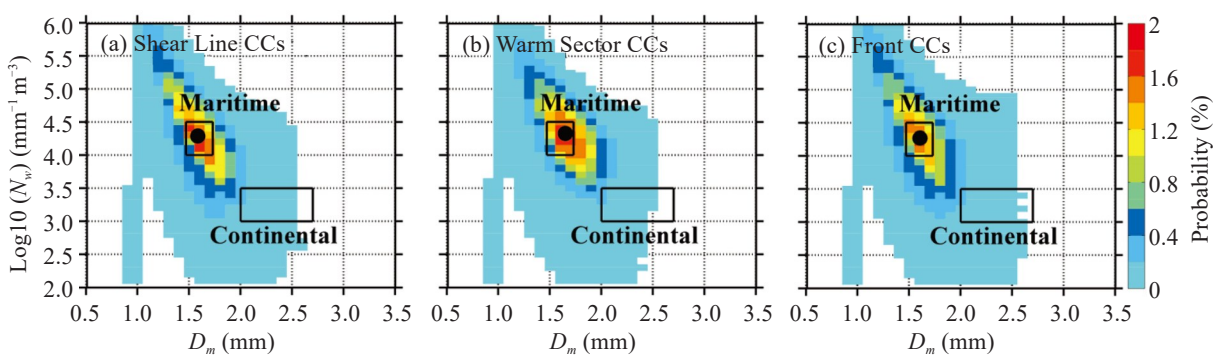

Figure 10. Joint probability density distribution of D_m (units: mm) and $\log_{10}N_w$ (units: mm^{-1} m^{-3}) of the CCs for the three types of rainfall of (a) SR, (b) WR, and (c) FR.

and FR.

Figure 11 shows the average distribution of the vertical profiles of D_m and N_w retrieved from radar observations for the three types of heavy rainfall below 4 km in height. The vertical profiles of D_m and N_w were considerably different for the three types of rainfall. The mean D_m of WR and FR increased with decreasing altitude, especially for WR. In contrast, the mean values

of $\log_{10}N_w$ for WR and FR decreased with the height decreasing. These confirm again that for both WR and FR, and especially for WR, there was a clear coalescence process during the falling process. The mean value of D_m in the SR showed a decreasing trend from the height of 4 km to 2.5 km, but the transition was less pronounced below 2.5 km. The mean value of $\log_{10}N_w$ for SR showed an increasing trend from 4 km to 1.5 km and then decreased. This also suggests that for SR below 3 km, fragmentation and coalescence

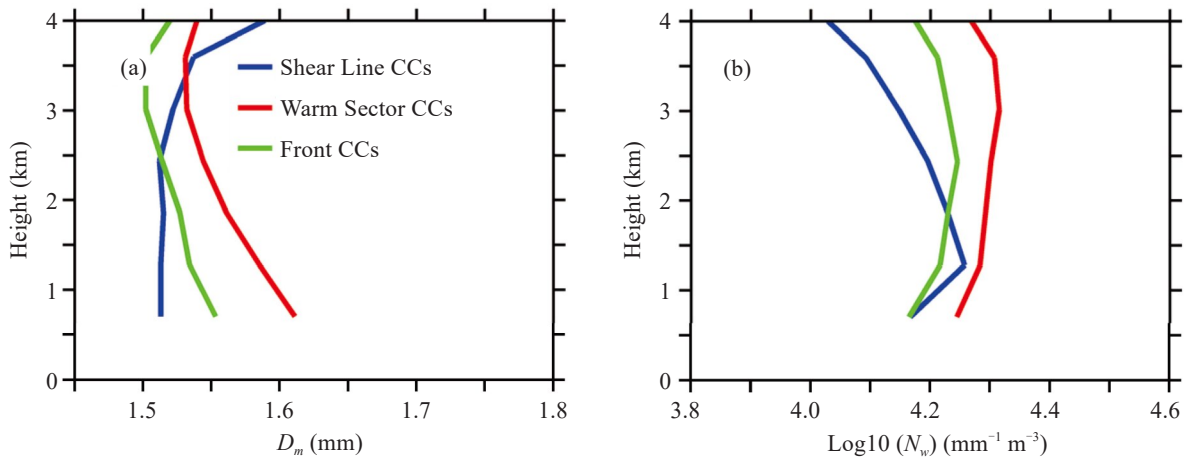

Figure 11. Mean profiles of the retrieved (a) D_m (units: mm) and (b) $\log_{10}N_w$ (units: mm^{-1} m^{-3}) of the CCs. Solid blue, red, and green lines represent the SR, WR, and FR, respectively.

processes might tend to be in equilibrium.

As shown in Fig. 12, the vertical profile of the LWC (units: g m^{-3}) and IWC (units: g m^{-3}) of CCs for the three types of rainfall were determined according to different maximum Z_H classification, (a) 40−45 dBZ, (b) 45−50 dBZ, and (c) >50 dBZ. For each Z_H classification, the LWC and IWC in the WR had the highest vertical content at all height levels, followed by the FR and SR. In particular, when maximum Z_H >50 dBZ (Fig. 12c), the IWC in the WR reached a maximum of 1.3 g m^{-3} above the 0 ℃ level, suggesting that the ice-phase process was active. The LWC in the WR reached a maximum of 4.8 g m^{-3} below the 0 ℃ level, indicating that the IWC accounted for about 27% of LWC during the falling process for the WR. Correspondingly, when maximum Z_H >50 dBZ, the IWC accounted for about 22% and 20% of LWC during the rain process for the SR and FR, respectively. These suggest that the ice-phase process played a more prominent role in the WR systems than in the SR and FR, and can produce heavier rainfall. The IWC in the SR was the lowest of the three heavy rainfall systems, indicating that the ice-phase process was the least active.

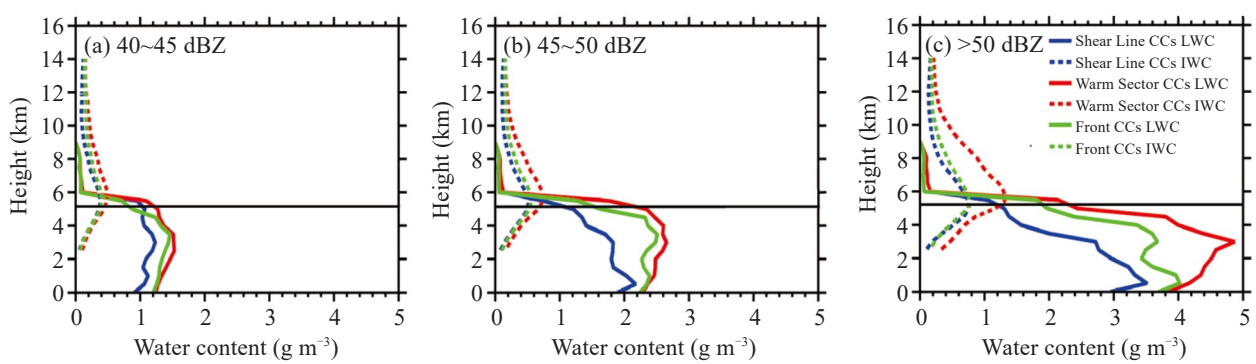

Figure 12. The vertical profile of LWC (units: g m^{-3}) and IWC (units: g m^{-3}) of CCs for the three types of rainfall according to different maximum Z_H classification for (a) 40-45 dBZ, (b) 45-50 dBZ, and (c) >50 dBZ. The blue, red, and green solid lines represent the LWC of SR, WR, and FR, respectively, and the solid black line indicates the 0 ℃ level.

The proportion of heavy rains in the WR (Fig. 13b) was obviously larger than in the FR and SR. Hence, the WR had the highest rainfall intensity. From 4 to 8 km in height, the average graupel ratio reached up to 26% in the WR (Fig. 13b), followed by the FR (Fig. 13c) (~20%), while the SR (Fig. 13a) was only 17%. Graupel occupied the maximum fraction in the WR, suggesting that its riming process was likely to be the most active. In general, more proportion of graupel in the rain, stronger updrafts, and more abundant water vapor supply might lead to larger-sized raindrops during the

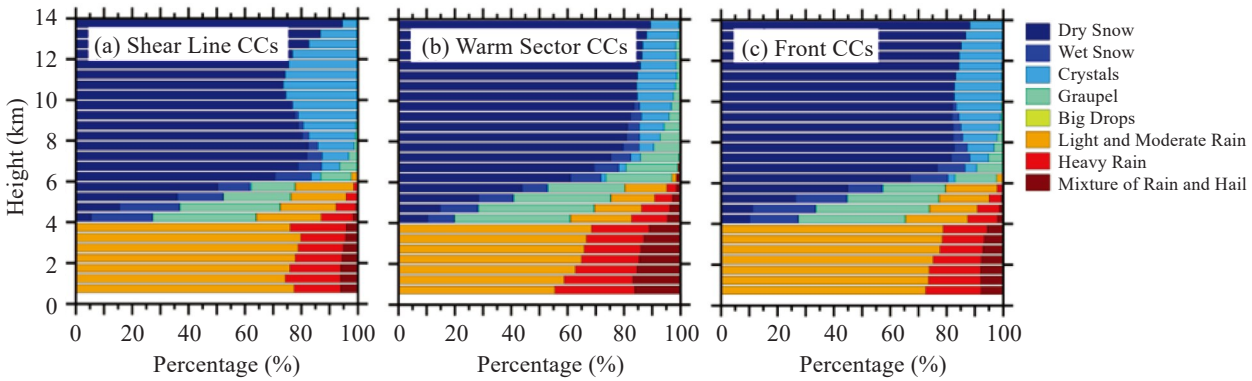

Figure 13. The stacked frequency (units: %) of each identified hydrometeor by altitude of the CCs for the three types of rainfall.

melting and collision-coalescence processes.

6 CONCLUSIONS AND DISCUSSION

During 10−15 May 2022, a heavy rainfall event occurred in south China, in which three types of rainfall (SR, WR, and FR) happened successively. In this study, based on the combined observations from 11 polarimetric radars, AWSs observations, ERA5 reanalysis, lightning observations, and the corresponding retrieval algorithms of microphysical characteristics of rainfall, we investigated the differences in the microphysical characteristics of these three rainfalls. The conclusions are as follows:

(1) Throughout the entire altitude range, the mean Z_H values of the CCs in the WR were higher than those in the SR and FR. The Z_H values of 20 dBZ reached the height of 18 km in the WR, followed by the FR and SR. The average area ratio of CCs was 6.2%, 4.6%, and 3.8% in the WR, FR, and SR, respectively. Meanwhile, the lightning densities in the WR were higher than those in the SR and FR. These indicate that the convection motion in the WR was the most vigorous, followed by the FR and SR. The mean K_{DP} in the WR was the largest below the 0 ℃ level, indicating that its rainfall intensity was also the largest. Below 3 km, there was likely an obvious coalescence process in the WR and FR. The breaking process in the SR balanced with the coalescence process below 3 km.

(2) The raindrop size distribution characteristics of the three types of heavy rainfall all belong to marine-type precipitation. The WR process had the highest proportion of graupel (26%), the most active riming and coalescence process. In addition, WR raindrops had the highest mean values of D_m and N_w compared to SR and FR. Moreover, the mean values of D_m and N_w for FR and SR were close to each other.

(3) The IWC of the WR was considerably higher than that of the SR and FR at all heights, and the lightning density was also the largest, indicating that the ice-phase process in the WR was likely the most active. The ice-phase process in the SR was the least active. The IWC in the WR accounted for about 27% of LWC when Z_H exceeded 50 dBZ, which is significantly higher than those in the SR (22%) and FR (20%). These suggest that the ice-phase process in the WR contributed higher liquid rainfall than in the SR and FR.

Based on the observations from multiple S-band polarimetric radars, we presented a detailed comparison of the vertical structures and microphysical characteristics of the WR, SR, and FR in south China in this study. However, this analysis only focuses on the process of heavy rainfall that occurred in May 2022, and a more in-depth study based on additional case statistics is needed.

Acknowledgments: We would like to acknowledge the Guangdong Meteorological Administration for collecting and archiving radar data, and the ECMWF for providing ERA5 reanalysis data used in this study.

REFERENCES

[1] ZHANG M R, RASMUSSEN K L, MENG Z Y, et al. Impacts of the coastal terrain on the warm-sector heavy-rain-producing MCSs in southern China [J]. Monthly Weather Review, 2022, 150(3): 603-624, https://doi. org / 10.1175/MWR-D-21-0190.1

[2] WU H Y, DU Y D, QIN P. Climate characteristics and variation of rainstorm in south China [J]. Meteorological Monthly, 2011, 37(10): 1262-1269 (in Chinese), https://doi. org/10.7519/j.issn.1000-0526.2011.10.009

[3] LIANG Q Q, MENG W G, SUN X Y, et al. Contrastive analysis of frontal rainstorm vs monsoon rainstorm processes during the April-May-June raining season vs July-August-September raining season [J]. Journal of Tropical Meteorology, 2019, 35(1): 51-62 (in Chinese), https://doi.org/10.16032/j.issn.1004-4965.2019.005

[4] LUO Y L, SUN J S, LI Y, et al. Science and prediction of heavy rainfall over China: Research progress since the reform and opening-up of the People's Republic of China [J]. Acta Meteorologica Sinica, 2020. 78(3): 419-450 (in Chinese), https://doi.org/10.11676/qxxb2020.057

[5] HUANG S S, LI Z G, BAO C L, et al. Rainstorms During Pre-Rainy Season in South China [M]. Guangzhou: Guangdong Science and Technology Press, 1986: 55-95 (in Chinese).

[6] HE L F, CHEN T, KONG Q. A review of studies on

prefrontal torrential rain in South China [J]. Journal of Applied Meteorological Science, 2016, 27(5): 559-569 (in Chinese), https://doi.org/10.11898/1001-7313.20160505

[7] SUN J H, ZHANG Y C, LIU R X, et al. A Review of research on warm-sector heavy rainfall in China [J]. Advances in Atmospheric Sciences, 2019, 36(12): 1299-1307, https://doi.org/10.1007/s00376-019-9021-1

[8] WU Y L, GAO Y D, CHEN D H, et al. Synoptic characteristics related to warm-sector torrential rainfall events in South China during the annually first rainy season [J]. Journal of Tropical Meteorology, 2020, 26(3): 253-260, https://doi.org/10.46267/j.1006-8775.2020.023

[9] ZHENG T F, YU X, HUANG J, et al. An observational analysis of a torrential rainstorm in the warm sector of South China coastal areas [J]. Journal of Tropical Meteorology, 2018, 24(4): 481-493, https://doi. org / 10.16555/j.1006-8775.2018.04.007

[10] YIN J F, WANG D H, LIANG Z M, et al. Numerical study of the role of microphysical latent heating and surface heat fluxes in a severe precipitation event in the warm sector over southern China [J]. Asia-Pacific Journal of Atmospheric Sciences, 2018, 54(1): 77-90, https://doi.org/10.1007/s13143-017-0061-0

[11] ZHONG S X, LI X Y, YANG S, et al. Characteristics and synoptic environment of torrential rain in the warm sector over South China: A composite study [J]. Meteorology and Atmospheric Physics, 2019, 131(5): 1191-1203, https://doi.org/10.1007/s00703-018-0629-y

[12] WU N G, WEN Z P, DENG W J, et al. Advances in warm-sector heavy rainfall during the first rainy season in South China [J]. Journal of the Meteorological Sciences, 2020, 40(5): 605-616 (in Chinese), https://doi. org / 10.3969 / 2020jms.0077

[13] LIANG Z M, LIU Y, YIN J F, et al. A case study of the effects of a synoptic situation on the motion and development of warm-sector mesoscale convective systems over South China [J]. Asia-Pacific Journal of Atmospheric Sciences, 2019, 55(2): 255-268, https://doi.org/10.1007/s13143-018-0063-6

[14] WU N G, ZHUANG X R, MIN J Z, et al. Practical and intrinsic predictability of a warm-sector torrential rainfall event in the south China monsoon region [J]. Journal of Geophysical Research: Atmospheres, 2021, 125(4): e2019JD031313, https://doi.org/10.1029/2019JD031313

[15] ZHAO Y C, LI Z C, XIAO Z N. Comparison analysis of South China front and warm-area heavy rain systems in June 2006 [J]. Meteorological Science and Technology, 2008, 36(1): 47-54 (in Chinese), https://doi.org/10.19517/j.1671-6345.2008.01.011

[16] WANG H, LUO Y L, JOU B J D. Initiation, maintenance, and properties of convection in an extreme rainfall event during SCMREX: Observation analysis [J]. Journal of Geophysical Research: Atmospheres, 2014, 119(23): 13206-13232, https://doi.org/10.1002/2014JD022339

[17] LIN L X. Technical manual for Guangdong weather forecast [M]. Beijing: China Meteorological Press, 2006: 95-150 (in Chinese).

[18] ZHENG B, LIANG J Y, LIN A L, et al. Frontal rain and summer monsoon rain during pre-rainy season in South China. Part I: Determination of the division dates [J]. Chinese Journal of Atmospheric Sciences, 2006, 30(6): 1207-1216 (in Chinese), https://doi. org / 10.3878 / j. issn.1006-9895.2006.06.15

[19] LIU B Q, HE J H. Reviews on the dynamics of Asian summer monsoon [J]. Journal of Tropical Meteorology, 2015, 31(6): 869-880 (in Chinese), https://doi. org / 10.16032/j.issn.1004-4965.2015.06.015

[20] LARSON R N. Shear line weather regime over Hawaii [J]. Monthly Weather Review, 1976, 104(8): 1081-1083, https://doi. org / 10.1175 / 1520-0493(1976)104<1081: SLWROH>2.0.CO;2

[21] WEN J, ZHAO K, HUANG H, et al. Evolution of microphysical structure of a subtropical squall line observed by a polarimetric radar and a disdrometer during OPACC in Eastern China [J]. Journal of Geophysical Research: Atmospheres, 2017, 122(15): 8033-8050, https://doi.org/10.1002/2016JD026346

[22] HAN B, DU Y, WU C, et al. Microphysical characteristics of the coexisting frontal and warm-sector heavy rainfall in South China [J]. Journal of Geophysical Research: Atmospheres, 2021, 126(21): e2021JD035446, https://doi.org/10.1029/2021JD035446

[23] LAI R Z, LIU X T, HU S, et al. Raindrop size distribution characteristic differences during the dry and wet seasons in South China [J]. Atmospheric Research, 2022, 266: 105947, https://doi.org/10.1016/j.atmosres.2021.105947

[24] LI M X, LUO Y L, ZHANG D L, et al. Analysis of a record-breaking rainfall event associated with a monsoon coastal megacity of South China using multisource data [J]. IEEE Transactions on Geoscience and Remote Sensing, 2020, 59(8): 6404-6414, https://doi.org/10.1109/TGRS.2020.3029831

[25] FU P L, HU D M, ZHANG Y, et al. Microphysical characteristics, initiation and maintenance of record heavy rainfall over Guangzhou region on 7 May 2017 [J]. Meteorological Monthly, 2018, 44(4): 500-510 (in Chinese), https://doi. org / 10.7519 / j. issn. 1000-0526.2018.04.003

[26] HUANG H, ZHAO K, CHAN J C L, et al. Microphysical characteristics of extreme-rainfall convection over the pearl river delta region, south China from polarimetric radar data during the pre-summer rainy season [J]. Advances in Atmospheric Sciences, 2023, 40(5): 874-886, https://doi.org/10.1007/s00376-022-1319-8

[27] CHEN C, HU Z Q, HU S, et al. Preliminary analysis of data quality of Guangzhou S-band polarimetric weather radar [J]. Journal of tropical meteorology, 2018, 34(1): 59-67 (in Chinese), https://doi. org / 10.16032 / j. issn. 1004-4965.2018.01.006

[28] CHEN C, LIU L P, HU S, et al. Operational evaluation of the quantitative precipitation estimation by a CINRAD-SA dual polarization radar system [J]. Journal of Tropical Meteorology, 2020, 26(2): 176-187, https://doi. org / 10.46267/j.1006-8775.2020.016

[29] XIA F, LIU X T, ZHENG T F, et al. Correction of rainfall attenuation and partial terrain blockage for C band dual-polarization weather radar [J]. Journal of Tropical Meteorology, 2021, 37(4): 556-568 (in Chinese), https://doi.org/10.16032/j.issn.1004-4965.2021.053

[30] LIU X T, WAN Q L, WANG H, et al. Raindrop size distribution parameters retrieved from Guangzhou S-band polarimetric radar observations [J]. Journal of Meteorological Research, 2018, 32(4): 571-583, https://doi.org/10.1007/s13351-018-7152-4

[31] LI M F, MIN C, ZHANG A S, et al. Analysis of CINRAD coverage in Guangdong Province based on SRTM data [J]. Journal of Geo-Information Science, 2018, 20(8): 1201-1208, https://doi.org/10.12082/dqxxkx.2018.180121

[32] WU C, LIU L P, WEI M, et al. Statistics-based optimization of the polarimetric radar hydrometeor classification algorithm and its application for a squall line in South China [J]. Advances in Atmospheric Sciences, 2018, 35(3): 296-316, https://doi.org/10.1007/s00376-017-6241-0

[33] WANG H, KONG F Y, WU N G, et al. An investigation into microphysical structure of a squall line in South China observed with a polarimetric radar and a disdrometer [J]. Atmospheric Research, 2019, 226: 171-180, https://doi.org/10.1016/j.atmosres.2019.04.009

[34] YU S T, LUO Y L, WU C, et al. Convective and microphysical characteristics of extreme precipitation revealed by multisource observations over the Pearl River Delta at monsoon coast [J]. Geophysical Research Letters, 2022, 49(2): e2021GL097043, https://doi. org / 10.1029/2021GL097043

[35] LIU X T, RUAN Z, HU S, et al. The Longmen Cloud Physics Field Experiment Base, China Meteorological Administration [J]. Journal of Tropical Meteorology, 2023, 29(1): 1-15, https://doi. org / 10.46267 / j. 1006-8775.2023.001

[36] FENG L, HU S, LIU X T, et al. Precipitation microphysical characteristics of typhoon mangkhut in southern China using 2D video disdrometers [J]. Atmosphere, 2020, 11(9): 975, https://doi. org / 10.3390 / atmos11090975

[37] FENG L, LIU X T, XIAO H, et al. Characteristics of raindrop size distribution in Typhoon Nida (2016) before and after landfall in southern China from 2D video disdrometer data [J]. Advances in Meteorology, 2021, 349738, https://doi.org/10.1155/2021/9349738

[38] DING Y, WAN Q L, YANG L, et al. Raindrop size distribution parameters retrieved from Xinfeng C-Band polarimetric radar observations [J]. Journal of Tropical Meteorology, 2020, 26(3): 275-285, https://doi. org / 10.46267/j.1006-8775.2020.025

[39] LI H Q, WAN Q L, PENG D D, et al. Multiscale analysis of a record-breaking heavy rainfall event in Guangdong, China [J]. Atmospheric Research, 2020, 232: 104703, https://doi.org/10.1016/j.atmosres.2019.104703

[40] PARK H S, RYZHKOV A V, ZRNIĆ D S, et al. The hydrometeor classification algorithm for the polarimetric WSR-88D: Description and application to an MCS [J]. Weather and Forecasting, 2009, 24(3): 730-748, https://doi.org/10.1175/2008waf2222205.1

[41] GUO Z Y, HU S, LIU X T, et al. Improving S-band polarimetric radar monsoon rainfall estimation with two-dimensional video disdrometer observations in South China [J]. Atmosphere, 2021, 12(7): 831, https://doi.org/10.3390/atmos12070831

[42] ZHOU X Y, HU D M, ZHANG Y, et al. Reliability of X-band Dual-polarization phased array radars through comparison with an S-band dual-polarization doppler radar [J]. Journal of Tropical Meteorology, 2022, 28(2): 218-236, https://doi.org/10.46267/j.1006-8775.2022.017

Citation: XIA Feng, LIU Xian-tong, HU Sheng, et al. Comparison of Microphysical Characteristics of Warm-sector, Frontal and Shear-line Heavy Rainfall During the Pre-summer Rainy Season in South China [J]. Journal of Tropical Meteorology, 2023, 29(2): 204-215, https://doi.org/10.46267/j.1006-8775.2023.016